JBC RESEARCH ARTICLE

Contrasting functions of ATP hydrolysis by MDA5 and LGP2 in viral RNA sensing

Received for publication, August 30, 2023, and in revised form, January 16, 2024 Published, Papers in Press, February 1, 2024,
https://doi.org/10.1016/j.jbc.2024.105711

Rahul Singh[1,2,3], **Yuan Wu**[1,2], **Alba Herrero del Valle**[1,2], **Kendra E. Leigh**[1,2], **Sai Mong**[1,2], **Mark T. K. Cheng**[1,2], **Brian J. Ferguson**[3,*], **and Yorgo Modis**[1,2,*]

From the [1]*Molecular Immunity Unit, Department of Medicine, University of Cambridge, MRC Laboratory of Molecular Biology, Cambridge, UK;* [2]*Cambridge Institute of Therapeutic Immunology & Infectious Disease (CITIID), Department of Medicine, and* [3]*Department of Pathology, University of Cambridge, Cambridge, UK*

Reviewed by members of the JBC Editorial Board. Edited by Craig Cameron

Cytosolic long dsRNA, among the most potent proinflammatory signals, is recognized by melanoma differentiation-associated protein 5 (MDA5). MDA5 binds dsRNA cooperatively forming helical filaments. ATP hydrolysis by MDA5 fulfills a proofreading function by promoting dissociation of shorter endogenous dsRNs from MDA5 while allowing longer viral dsRNAs to remain bound leading to activation of interferon-β responses. Here, we show that adjacent MDA5 subunits in MDA5-dsRNA filaments hydrolyze ATP cooperatively, inducing cooperative filament disassembly. Consecutive rounds of ATP hydrolysis amplify the filament footprint, displacing tightly bound proteins from dsRNA. Our electron microscopy and biochemical assays show that LGP2 binds to dsRNA at internal binding sites through noncooperative ATP hydrolysis. Unlike MDA5, LGP2 has low nucleic acid selectivity and can hydrolyze GTP and CTP as well as ATP. Binding of LGP2 to dsRNA promotes nucleation of MDA5 filament assembly resulting in shorter filaments. Molecular modeling identifies an internally bound MDA5-LGP2-RNA complex, with the LGP2 C-terminal tail forming the key contacts with MDA5. These contacts are specifically required for NTP-dependent internal RNA binding. We conclude that NTPase-dependent binding of LGP2 to internal dsRNA sites complements NTPase-independent binding to dsRNA ends, *via* distinct binding modes, to increase the number and signaling output of MDA5-dsRNA complexes.

Viruses deliver or generate RNA in the host cell cytosol for viral gene expression by cellular machinery. When present in the cytosol, dsRNAs are one of the most potent proinflammatory pathogen associated molecular patterns (1). The antiviral innate immune responses induced by dsRNA sensors must be sensitive enough to detect infection and specific enough to avoid activation by cellular RNA. Failure to balance sensitivity with specificity can lead to viral proliferation or autoinflammatory disease (2). The primary sensors of cytosolic dsRNA in vertebrates are RIG-I (3, 4), melanoma differentiation-associated protein 5 (MDA5) (4–6), LGP2 (7–11), often referred to as the RIG-I-like receptors, and protein kinase R (12, 13). These are complemented in mammals by the oligoadenylate synthase family of proteins (14, 15) as well as ZBP1, and in humans, NLRP1 (16). MDA5 recognizes dsRNAs longer than 100 bp(5, 6) and binds dsRNA cooperatively, forming helical filaments with its RIG-I-like superfamily 2 helicase module and C-terminal domain (CTD) (17–22). This filament formation induces the tandem caspase recruitment domains (CARDs) of MDA5 to form oligomers (17, 18). These MDA5 CARD oligomers recruit mitochondrial antiviral signaling protein *via* CARD-CARD interactions, nucleating the assembly of mitochondrial antiviral signaling protein CARD into microfibrils (23, 24), which activate potent interferon-β and NF-κB inflammatory responses (5, 6, 23).

MDA5 is the primary innate immune sensor for many viruses (5, 6), including SARS-CoV-2 (25, 26), but efficient proofreading and finely tuned signal transduction are necessary for a measured response to infection. Structural studies have shown that ATP hydrolysis by MDA5 performs a mechanical proofreading function (21, 22). The ATPase cycle is coupled to conformational changes in MDA5-dsRNA filaments that test the interactions of MDA5 with the bound RNA, promoting dissociation of MDA5 from endogenous RNAs with shorter or imperfect double-stranded regions, while allowing MDA5 to remain bound to longer virus-like dsRNAs long enough to activate signaling (21, 22). A-to-I deamination of dsRNA by adenosine deaminase RNA-specific (ADAR1), which weakens base pairing and causes bulges, is nevertheless required to prevent MDA5-dependent autoinflammatory signaling induced by endogenous RNAs with high double-stranded content, for example, annealed inverted Alu repeats (27–30). MDA5 mutations that disrupt proofreading, for example, by inhibiting ATP hydrolysis, or otherwise increase baseline interferon signaling have been linked to autoinflammatory disorders in heterozygous human patients, including Aicardi–Goutières syndrome, Singleton–Merten syndrome, spastic-dystonic syndrome, and neuroregression (31–33).

The conformational changes in MDA5-dsRNA filaments associated with ATP hydrolysis appear to fulfill other functions in addition to proofreading. ATP hydrolysis causes a 1-bp expansion of the RNA binding footprint of MDA5 from 14 to 15 base pairs (21). If adjacent MDA5 subunits in a filament hydrolyze

* For correspondence: Brian J. Ferguson, bf234@cam.ac.uk; Yorgo Modis, ymodis@mrc-lmb.cam.ac.uk.
Present address for Yuan Wu: Department of Biochemistry, University of Cambridge, Cambridge CB2 1QW, UK.

ATP in a sequential or cooperative manner, this RNA footprint expansion would be amplified. Expansion of the dsRNA footprint could explain the reported capacity of MDA5 to repair filament discontinuities and displace viral proteins from dsRNA in an ATPase-dependent, CARD-independent manner (34, 35). Indeed, ATP hydrolysis by RIG-I promotes assembly of signaling-active oligomers through local translocation, or threading of successive RIG-I monomers onto dsRNA ends (36, 37). However, whether ATP hydrolysis in adjacent MDA5 filament subunits is cooperative and drives expansion of the RNA footprint of MDA5 remains to be determined.

Multiple cofactors further increase the sensitivity and selectivity of MDA5-RNA recognition. LGP2, arguably the most important MDA5 cofactor, promotes MDA5 filament formation on dsRNA (10, 38–41). LGP2 contains a DExD/H-box helicase and CTD similar to those of MDA5 but lacks CARDs. Structural studies show that the LGP2 CTD can bind dsRNA blunt ends (8–10), while allowing short 5′ or 3′ overhangs and 5′-triphosphorylation to be accommodated (10). LGP2 RNA end binding has been proposed to nucleate MDA5 oligomerization on short (or otherwise suboptimal) dsRNAs (10, 42). LGP2 has also been found incorporated within MDA5 filaments, accelerating MDA5 filament formation and resulting in more numerous, shorter filaments that retain signaling activity (40, 41). The ATPase activity of LGP2 has been reported to promote dissociation of MDA5 from RNA (41), but a separate study reported that ATP hydrolysis by LGP2 enhances LGP2 RNA binding and hence promotes MDA5 signaling (39). It remains unclear, therefore, whether LGP2 interacts directly with MDA5, or exactly how the RNA binding and ATPase activities of LGP2 contribute to sensitive and selective dsRNA recognition by MDA5.

Here, we use a combination of electron microscopy and biochemical assays to show that adjacent MDA5 subunits hydrolyze ATP cooperatively within MDA5-dsRNA filaments and furthermore that RNA footprint expansion from this cooperative ATP hydrolysis within MDA5-RNA filaments can displace tightly bound proteins from dsRNA. We show that at higher concentrations, LGP2 competes with MDA5 for dsRNA binding, indicating that LGP2 can bind dsRNA internally, as well as at the ends. Unlike MDA5, LGP2 has low nucleic acid selectivity and hydrolyzes CTP and GTP as well as ATP. Nucleotide hydrolysis by LGP2 is noncooperative and coupled to dsRNA binding at internal binding sites. Molecular modeling of the MDA5-LGP2 interface with AlphaFold and site-directed mutagenesis based on the model suggests that the C-terminal tail of LGP2 is required to recruit MDA5 to internal sites on dsRNA rather than from dsRNA ends. Our work explains the ATP-dependent, interferon-independent antiviral activity of MDA5 and suggests that LGP2 amplifies MDA5 signaling by promoting the formation of stable MDA5 filaments.

Results

Adjacent subunits in MDA5-dsRNA filaments hydrolyze ATP cooperatively

The ATPase activity of MDA5 has been reported to fulfill additional functions other than proofreading, including repair of filament discontinuities and displacement of viral proteins from dsRNA (34, 35), but the molecular basis for these functions remains unknown. ATP hydrolysis causes a 1-bp expansion of the RNA binding footprint of MDA5 (21) so we hypothesized that adjacent MDA5 subunits in a filament may hydrolyze ATP sequentially or cooperatively and hence amplify this RNA footprint expansion sufficiently to close gaps in filaments and displace other RNA-bound proteins. To determine whether ATP hydrolysis is cooperative, we measured the ATPase activity of mouse MDA5-dsRNA filaments containing increasing proportions of the ATPase deficient MDA5 R338G mutant (corresponding to R337G in humans (32)), which has 8% of WT ATPase activity but can still bind and form filaments on dsRNA (Figs. 1, *A* and *B* and S1*A*). An analogous approach was used to detect sequential ATP hydrolysis in the hexameric ATPase FtsK (43). If MDA5 subunits hydrolyzed ATP independently, the loss of filament ATPase activity would be expected to be proportional to the amount of ATPase-deficient mutant incorporated. Instead, the ATPase activity dropped exponentially with increasing amounts of ATPase-deficient mutant, with MDA5-dsRNA filaments containing 20% of the ATPase-deficient mutant having less than half the ATPase activity of WT MDA5 filaments (Fig. 1*A*). The ATPase activity of WT MDA5-dsRNA complexes also increased exponentially as a function of increasing MDA5 concentration, reflecting the cooperativity of both filament assembly and ATP hydrolysis (Fig. 1*B*). In contrast, the ATPase activity of an MDA5 mutant with mutations that prevent filament formation, L397A/K398A/I399A (21), was directly proportional to the concentration of the MDA5 mutant, indicating noncooperative ATP hydrolysis (Fig. 1*B*). The ATPase activity of apyrase, which is monomeric in solution, was measured to provide a reference curve for noncooperative ATPase activity (Fig. S1*B*). Together, these data indicate that ATP hydrolysis in WT MDA5 filaments is cooperative, and that this cooperativity depends on filament formation.

MDA5 ATP hydrolysis displaces streptavidin from biotinylated dsRNA

A predicted consequence of cooperative ATP hydrolysis in MDA5-dsRNA filaments is that adjacent MDA5 subunits will hydrolyze ATP sequentially, causing a wave of ATP hydrolysis to spread along the filament or a segment thereof. This process could amplify the 1-bp RNA footprint expansion that accompanies each round of ATP hydrolysis and hence potentially displace any proteins bound to the RNA. To test this hypothesis, we generated 1-kb dsRNA containing a small fraction of internally incorporated or 3′-end incorporated biotinylated nucleotides, allowed streptavidin tetramers to bind to the biotin moieties, and asked whether MDA5 could displace the streptavidin from the RNA. Similar approaches were used previously to detect translocation of RIG-I and other helicases along nucleic acid duplexes (36, 44). Displacement was detected in electrophoretic mobility shift assays (Fig. 1*C*). Densitometry of the gel band corresponding

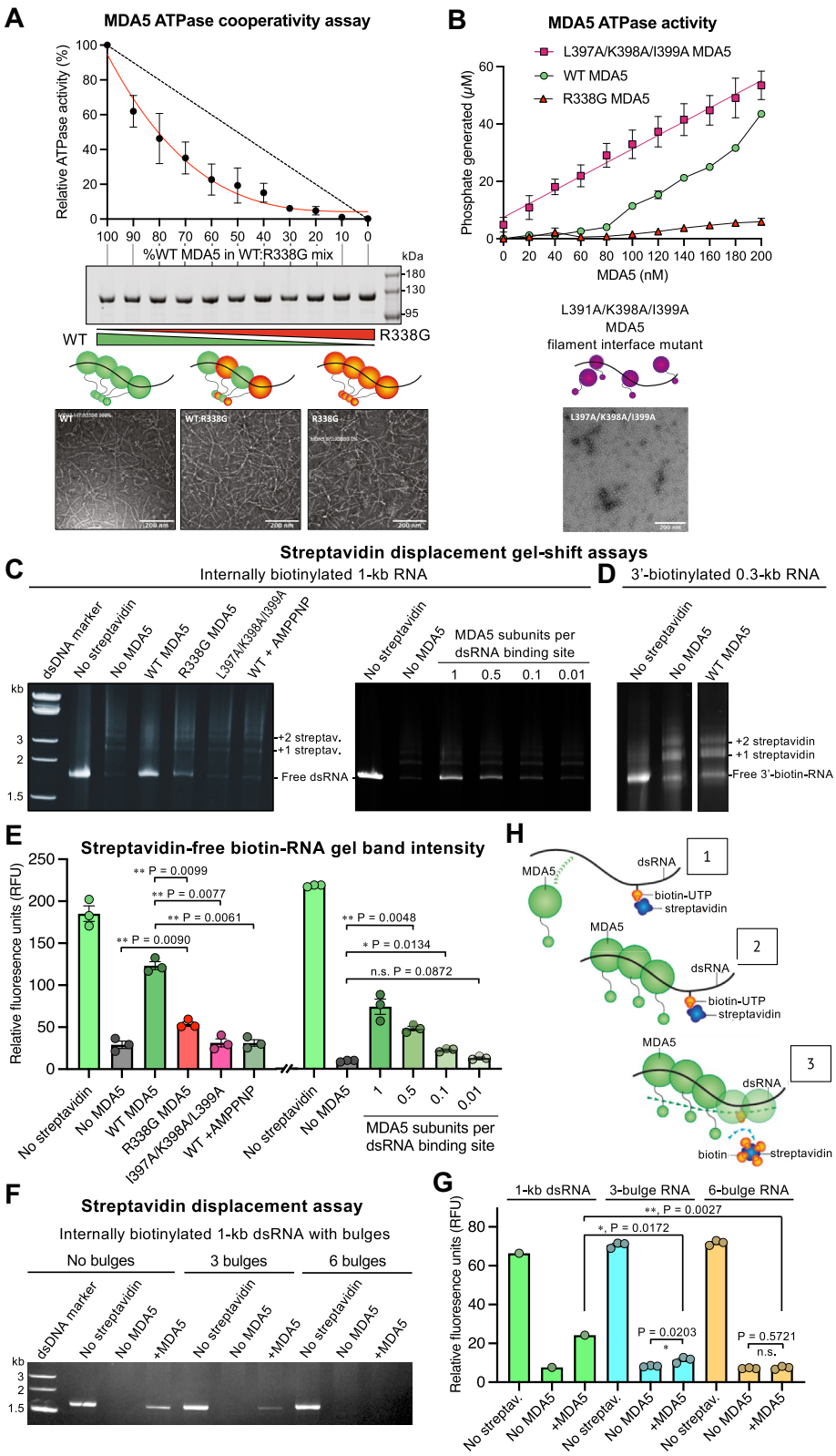

Figure 1. ATPase cooperativity and streptavidin displacement assays for MDA5-dsRNA filaments. *A*, ATPase activity of mouse MDA5-dsRNA filaments containing increasing proportions of the R338G MDA5 variant, which is ATPase deficient (Fig. S1*A*). *Dashed line*, the linear relationship expected in the absence of cooperativity. *Middle panel*: Coomassie-stained SDS-PAGE gel showing the total protein in each reaction mixture. *Bottom panel*: negative-stain electron micrographs of WT MDA5, a 1:1 WT:R338G MDA5 mix, and R338G MDA5 in the presence of 1-kb dsRNA. The scale bars represent 200 nm. *B*, *Left*, ATPase activity of MDA5-dsRNA complexes as a function of MDA5 concentration. *Right*, negative-stain electron micrograph of the filament interface mutant in the presence of 1-kb dsRNA. The scale bar represents 200 nm. *C* and *D*, polyacrylamide gel-shift assay for displacement of streptavidin from internally biotinylated dsRNA, (*C*), or 3′-biotinylated dsRNA (*D*). Samples were incubated in semidenaturing conditions (see Experimental procedures) to displace MDA5 but not streptavidin from the RNA. One MDA5 binding site was defined as 15 bp of dsRNA. *E*, quantification of streptavidin-free internally biotinylated

to streptavidin-free biotinylated RNA was used to quantify displacement (Fig. 1*E*). We found that MDA5 could displace streptavidin from internally biotinylated dsRNA in the presence of ATP (Fig. 1*C*, left panel). No streptavidin displacement was observed from 3′-end biotinylated dsRNA (Fig. 1*D*), or when the nonhydrolyzable ATP analog AMPPNP was used in place of ATP (Fig. 1*C*, left panel, last lane). Efficient streptavidin displacement required a molar excess of MDA5 relative to the number of 15-bp dsRNA binding sites (Fig. 1*C*, right panel), consistent with limited filament formation and ATP hydrolysis at small MDA5 to RNA molar ratios (Fig. 1*B*). The monomeric, ATPase-active MDA5 mutant L397A/K398A/I399A was unable to displace streptavidin, confirming that streptavidin displacement requires both filament formation and ATP hydrolysis (Fig. 1*C*, left panel). The ATPase-deficient MDA5 mutant R338G had low but detectable streptavidin displacement activity (Fig. 1*C*, left panel), consistent with the residual ATPase activity of this mutant (8% of WT MDA5). To assess the effect of interruptions in the RNA duplex on streptavidin displacement by MDA5, we introduced single-nucleotide bulges at regular intervals along one of the strands of the 1-kb dsRNA. Streptavidin displacement and filament formation were both significantly decreased in the presence of three bulges 250 bases apart, and completely abolished in the presence of six bulges 140 bases apart (Figs. 1, *F* and *G* and S1*C*). We conclude that cooperative ATP hydrolysis allows MDA5 filaments to displace tightly bound proteins from dsRNA by amplifying the RNA footprint expansion that accompanies each round of ATP hydrolysis by a single filament subunit (Fig. 1*H*). Moreover, continuous MDA5 filaments covering more than 250 bp of uninterrupted dsRNA, corresponding to 18 or more MDA5 subunits (based on MDA5's 14-bp footprint), are required to efficiently displace tightly bound proteins from RNA.

ATP hydrolysis by LGP2 is noncooperative and required for internal dsRNA binding

ATP hydrolysis by LGP2 had been reported to enhance binding of LGP2 to RNA and thus promote MDA5 signaling (39), but a subsequent study reported that the ATPase activity of LGP2 promoted dissociation of MDA5 from RNA (41). We applied negative-stain electron microscopy (ns-EM) and biochemical assays to clarify the role of ATP hydrolysis by LGP2 in RNA binding and MDA5 filament formation. Ns-EM of LGP2 and dsRNA in the absence of MDA5 showed that LGP2 can bind to internal dsRNA binding sites but does not form continuous filaments (Fig. 2*A*). Moreover, the LGP2 mutant R32G, which has 4% of WT LGP2 ATPase activity, was partially deficient for internal RNA binding (Figs. 2*A* and S1*A*). LGP2 mutant K30G, which lacks ATPase activity, failed to bind RNA internally. Consistent with this, bio-layer interferometry (BLI) data showed that the LGP2 K30G mutant had a 20-fold lower binding affinity for 1-kb dsRNA than WT LGP2, with a K_d of 1.3 μM for K30G *versus* 70 nM for WT (Fig. 2*B*). Similar differences in relative binding affinities were observed with a 300-bp dsRNA and a 40-nt ssRNA, with lower binding affinities for the LGP2 mutants as expected (Fig. S2*A*). We detected no basal ATPase activity in LGP2 in the absence of nucleic acids (Fig. 3*A*), in contrast to a previous study (39), but consistent with two other studies (10, 41). Together our data show that ATP hydrolysis by LGP2 promotes dsRNA binding and specifically is required for stem binding to internal dsRNA sites.

The ATPase activity of LGP2-dsRNA complexes containing increasing proportions of the ATPase-deficient R32G mutant decreased proportionally to the amount of the mutant present, indicating that ATP hydrolysis by LGP2 is noncooperative, in contrast to MDA5 (Fig. 2*C*). Accordingly, LGP2 failed to displace streptavidin from internally biotinylated dsRNA or 3′-end biotinylated dsRNA (Fig. 2*D*). Moreover, streptavidin displacement by MDA5 was unaffected by the addition of LGP2, implying that cooperative ATP hydrolysis by MDA5 filaments was unaffected by LGP2 (Fig. 2*D*). The net ATPase activities of different mixtures of WT LGP2, LGP2 K30G, or LGP2 R32G and MDA5, with dsRNA in excess, were furthermore consistent with the ATPase activities of MDA5 and LGP2 being independent and additive, rather than cooperative (Fig. 2*E*).

LGP2 has low selectivity for nucleic acids and is a semiselective NTPase

LGP2 is required to induce MDA5 signaling from RNAs with short or imperfect duplex regions, such as endogenous RNAs that escape editing by ADAR1 (42), suggesting that LGP2 has a broader RNA binding specificity than MDA5. The apparent binding affinity of LGP2 for 1-kb dsRNA from BLI was 20-fold higher than that of MDA5, with K_d values of 70 nM and 1.3 μM, respectively (Fig. 2*B*). Regarding nucleic acid binding specificity, we found that 100-bp dsRNA, and a 1-kb DNA:RNA hybrid induced similar levels of ATP hydrolysis by LGP2 as long (1 kb or 4 kb) linear dsRNA (Fig. 3*A*). Moreover, 100-bp dsDNA, 1-kb dsDNA, and 1-kb ssRNA induced 75 to 80% of the LGP2 ATPase activity observed with dsRNA. In contrast, of the nucleic acid species listed above, only long dsRNAs induced ATPase activity by MDA5 (Fig. 3*A*), although both MDA5 and LGP2 formed complexes with DNA:RNA hybrids to a similar extent as with dsRNA in gel shift assays (Fig. 3*B*). Three synthetic long (1400-, 2300-, and 2600-nt) ssRNAs predicted to have complex secondary structures with high base-paired content

RNA from gel band densitometry. Error bars show the s.e.m. of three independent experiments including the gels shown in (*C*). Statistical test: paired two-tailed *t* test, n = 3. See Supporting information for source data. *F*, polyacrylamide gel-shift assay for displacement of streptavidin from internally biotinylated 1-kb dsRNA with 0, 3, or 6 single-nucleotide bulges. *G*, quantification of streptavidin-free RNA from gel band densitometry. Error bars show the s.e.m. of three independent experiments including the gel shown in (*F*). Statistical test: unpaired two-tailed *t* test, n = 3 (bulged dsRNA) or n = 1 (1-kb RNA). See Supporting information for source data. *H*, proposed mechanism of streptavidin displacement from biotinylated RNA by cooperative ATP hydrolysis within MDA5 filaments. MDA5, melanoma differentiation-associated protein 5.

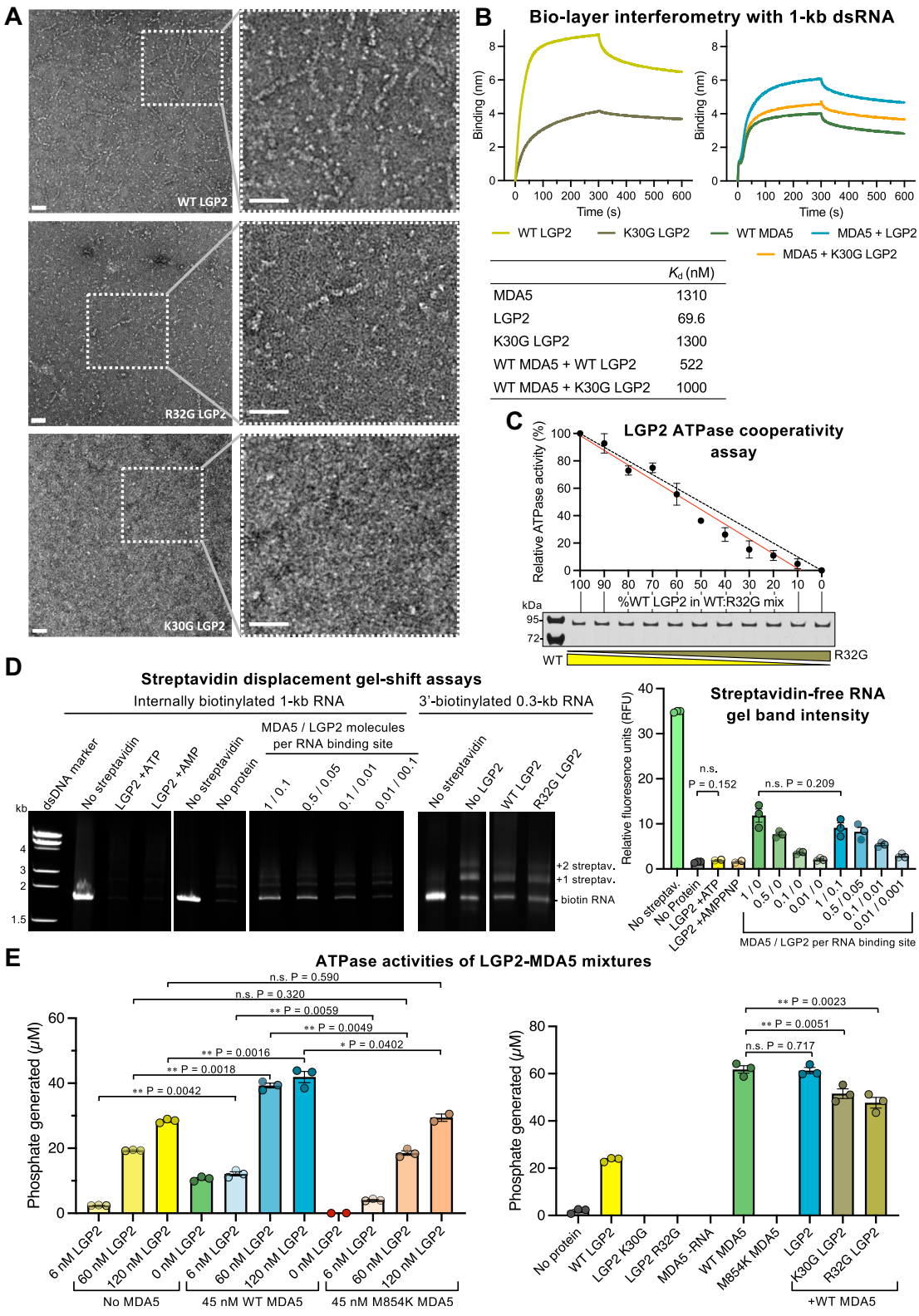

	K_d (nM)
MDA5	1310
LGP2	69.6
K30G LGP2	1300
WT MDA5 + WT LGP2	522
WT MDA5 + K30G LGP2	1000

Figure 2. RNA binding, ATPase cooperativity, and streptavidin displacement assays with LGP2 and LGP2-MDA5 mixtures. *A*, negative-stain electron micrographs of LGP2 (WT, R32G, and K30G variants) with 1-kb dsRNA. The scale bars represent 50 nm. *B*, bio-layer interferometry with 1-kb 3′-biotinylated dsRNA immobilized on a streptavidin biosensor and MDA5, LGP2, or MDA5-LGP2 mixtures in the mobile phase. Binding curves with immobilized 300-bp dsRNA and 40-nt ssRNA are shown in Fig. S1*B*. Dissociation constants derived from the curves are tabulated below. *C*, ATPase activity of mouse LGP2-dsRNA filaments containing increasing proportions of the R32G LGP2 variant, which is ATPase deficient (Fig. S1*A*). *Lower panel*: Coomassie-stained SDS-PAGE gel showing the total protein in each reaction mixture. *D*, polyacrylamide gel-shift assay for displacement of streptavidin from biotinylated dsRNA. Samples were incubated in semidenaturing conditions (See Experimental procedures) to displace MDA5 and LGP2 but not streptavidin from the RNA. The control lanes in the second panel from the *left* are also shown in Figure 1*C* (*right panel*). One binding site was defined as 15 bp of dsRNA. *Right panel*, quantification of streptavidin-free internally biotinylated RNA from gel band densitometry. The first six bars are also shown in Figure 1*E*. *E*, ATPase activities assay of different variants of LGP2 and MDA5 and their mixtures, with dsRNA binding sites in excess. The concentration of 15-bp dsRNA binding sites was 313 nM. Panels *C*–*E*: error bars show the s.e.m. of three independent experiments; statistical test: paired two-tailed *t* test, n = 3. See Supporting information for source data. MDA5, melanoma differentiation-associated protein 5.

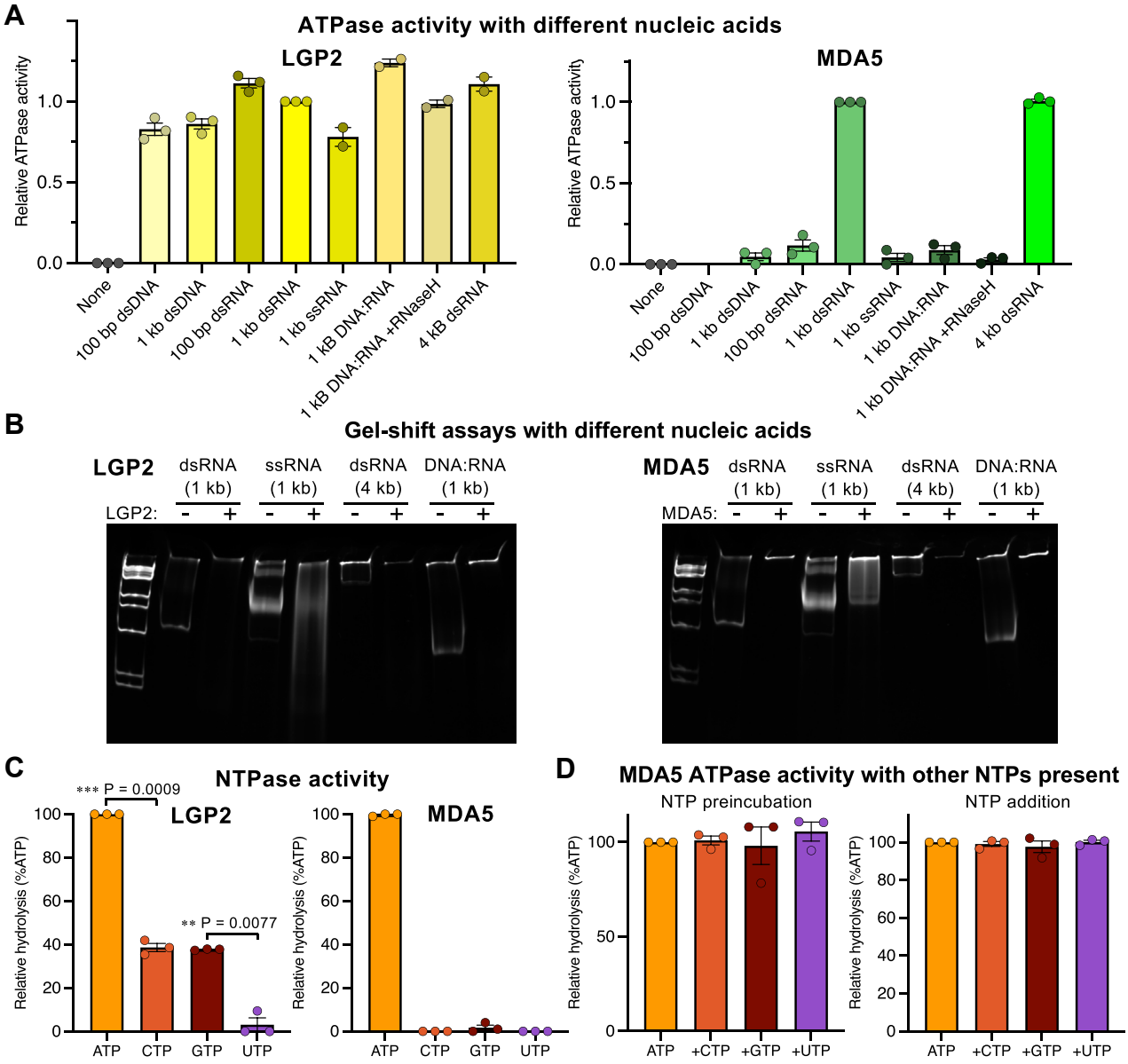

Figure 3. Nucleic acid and NTP selectivity for LGP2 and MDA5. *A*, ATPase activity of LGP2 and MDA5 in the presence of different nucleic acid ligands, expressed as the relative activity normalized to the condition with 1-kb dsRNA. Fig. S2 for ATPase activity of MDA5 in the presence of additional ligands. Error bars show the s.e.m. of two or three independent experiments. *B*, gel-shift assay for binding of LGP2 and MDA5 to different nucleic acid ligands. 4 to 20% polyacrylamide gels were used with 1 kb DNA Ladder (New England BioLabs cat. no. N3232S). See Fig. S2 for gel-shift assays with additional nucleic acid ligands. *C*, nucleotide hydrolysis activity of LGP2 and MDA5, expressed as percent of ATP hydrolysis activity. Error bars show the s.e.m. of three independent experiments. See Supporting information for source data. Statistical test: paired two-tailed *t* test, n = 3. *D*, ATPase activity of MDA5 following preincubation with or addition of CTP, GTP, or UTP in the presence of ATP. ATPase activity is not affected by the other nucleotides, demonstrating that they do not compete with ATP. Error bars show the s.e.m. of three independent experiments. MDA5, melanoma differentiation-associated protein 5.

induced similar levels of ATP hydrolysis by MDA5 as 1-kb dsRNA or Poly(I:C) (Fig. S3, *A* and *B*). MDA5 also formed filaments on these folded ssRNAs (Fig. S3, *C* and *D*), suggesting that MDA5 can also sense long ssRNAs, provided they fold into structures with sufficiently extensive base-paired regions.

Nucleotide hydrolysis assays showed that LGP2 is also less selective than MDA5 in its nucleotide utilization. LGP2 hydrolyzes CTP and GTP 40% as efficiently as ATP, in contrast to MDA5, which only hydrolyzes ATP (Fig. 3*C*). No UTP hydrolysis could be detected for either LGP2 or MDA5. Addition of CTP, GTP, or UTP did not affect MDA5 ATPase activity, demonstrating that the ATP binding pocket of MDA5 is selective for ATP (Fig. 3*D*). Although DEAH/RHA and NS3/NPH-II helicases from superfamily 2 hydrolyze all four types of NTPs (45, 46), the semiselective NTP hydrolysis observed here for LGP2 is unexpected given that MDA5 is selective for ATP. We note that RNA viruses have unusual genomic nucleotide

compositions (47) causing different NTPs to be consumed at different rates. This raises the question of whether LGP2 evolved its lower nucleotide selectivity as an adaptation to changes in the cellular nucleotide pool associated with infection.

LGP2 promotes nucleation of MDA5 filament assembly at internal dsRNA sites

Crystal structures of LGP2-RNA complexes identified dsRNA blunt ends as the preferred binding site for LGP2 (8–10) on dsRNA, but subsequent electron microscopy and atomic force microscopy studies suggested LGP2 can bind dsRNA internally as a stem binder (10, 41). ATP hydrolysis by LGP2 has been reported to enhance binding of LGP2 to RNA and hence promote MDA5 signaling (39). To gain further insight on how LGP2 may affect MDA5 filament formation we imaged filaments formed in the presence of LGP2, MDA5, and dsRNA by ns-EM. The electron micrographs showed that addition of increasing amounts of LGP2 to mixtures of MDA5 and dsRNA progressively reduced the average length of the resulting protein filaments (Fig. 4, *A* and *B*). This could in principle be attributed to increased MDA5 filament nucleation, reduced cooperativity of MDA5 filament assembly, or competition between MDA5 and LGP2 for dsRNA binding. The overall ATPase activity of filaments and their capacity to displace streptavidin from biotinylated internal nucleotides were not significantly affected by LGP2 when the number of RNA binding sites was not limiting (Fig. 2, *D* and *E*), indicating that LGP2 did not interfere with the cooperativity of filament assembly or ATP hydrolysis by MDA5 filaments. BLI with immobilized dsRNA and a molar excess of 15-bp dsRNA binding sites showed that an MDA5-LGP2 mixture had a slightly higher net dsRNA binding affinity than MDA5 alone, with apparent K_d values of 520 nM and 1.3 μM, respectively (Fig. 2*B*). This suggests that the reduction in MDA5 filament length caused by LGP2 is primarily due to increased MDA5 filament nucleation rather than competition between MDA5 and LGP2 for dsRNA binding. However, when the number of dsRNA binding sites was limiting, the net ATPase activity of mixed MDA5-LGP2 filaments decreased with increasing concentrations of LGP2 (Fig. 4*C*). Since the ATPase activity of LGP2 is one-third of that of MDA5 (Fig. 2*E*) and LGP2 has a higher binding affinity for dsRNA than MDA5 (Fig. 2*B*), this decrease in ATPase activity can be attributed to competition between LGP2 and MDA5 for dsRNA binding sites. Whether MDA5 or LGP2 dsRNA binding sites are limiting in infected cells remains unknown but given that MDA5 binds RNA more cooperatively and is expressed at higher levels than LGP2, both at baseline and upon induction by viral infection or interferon (4, 11), it seems unlikely that LGP2 would outcompete MDA5 for RNA binding in the cellular context. Overall, together with previous evidence that LGP2 amplifies MDA5 signaling (39–41), our data support the model that LGP2 promotes nucleation of MDA5 filaments—including at internal RNA sites with LGP2 ATP hydrolysis—resulting in shorter, more numerous filaments (Fig. 4*D*).

Molecular modeling of an LGP2-MDA5 complex with AlphaFold-Multimer

Nucleation of MDA5 filament assembly by LGP2 may depend on direct interactions between MDA5 and LGP2. We could not confirm the presence of such interactions experimentally because the two proteins have similar structures and could not be distinguished in our electron micrographs. We therefore generated atomic model predictions of MDA5-LGP2 complexes with AlphaFold-Multimer (48–50) as implemented by ColabFold (50). With only the sequences of human or mouse LGP2 and MDA5 as the input, AlphaFold generated LGP2-MDA5 complexes with high confidence scores (average pLDDT = 85–87). All the generated AlphaFold models had the same overall structure, with or without the use of model templates from the Protein Data Bank. The predicted LGP2-MDA5 interface resembled the MDA5-MDA5 interface in cryo-EM structures of helical MDA5-dsRNA filaments (21). Despite RNA modeling not being supported by AlphaFold, the models contained a central void, or channel along the helical axis where dsRNA should bind (Fig. 5, *A* and *B*). In all models, LGP2 and MDA5 were in a head-to-tail configuration, with the MDA5 pincer domain at the center of the filament-like interface. When a second molecule of MDA5 was added to the modeling input, the same LGP2-MDA5 heterodimer was predicted and the second MDA5 molecule was placed on the opposing filament forming face of the first MDA5 molecule to form a three-subunit filament with LGP2 at one end (Fig. 5*A*). Analysis with the proteins, interfaces, structures, and assemblies (PISA) server (51) showed that the predicted LGP2-MDA5 interface had a larger buried surface area and estimated solvation free energy gain when compared to the MDA5-MDA5 interfaces obtained by cryo-EM or predicted by AlphaFold (Fig. 5*C*).

In crystal structures of LGP2-RNA complexes, LGP2 is in end-binding mode (10). The capping loop (residues 591-602) in the CTD caps one end of the RNA while allowing 5′ or 3′ overhangs and 5′-triphosphorylation to be accommodated (Fig. 5*D*) (10). Internal or stem binding to dsRNA would require the capping loop to move away from the helical axis of the dsRNA (10). In our AlphaFold models, the conformation of LGP2 is similar to that of the crystal structures, but LGP2 is unexpectedly oriented with its capping loop facing (but not contacting) the interacting MDA5 subunit (Fig. 5*A*). This orientation means that the free end of an end-bound dsRNA would be located on the opposite side of LGP2, near the pincer domain and facing away from the MDA5 subunit. In the modeled conformation, the LGP2 capping loop partially occludes the dsRNA binding channel and would have to move away from the filament axis as previously proposed (10) to accommodate dsRNA in the stem binding mode (Fig. 5, *A* and *B*). The polarity of the MDA5-LGP2 interaction—with the LGP2 C-terminal tail (residues 663-677) forming most of the contacts with MDA5 and the LGP2

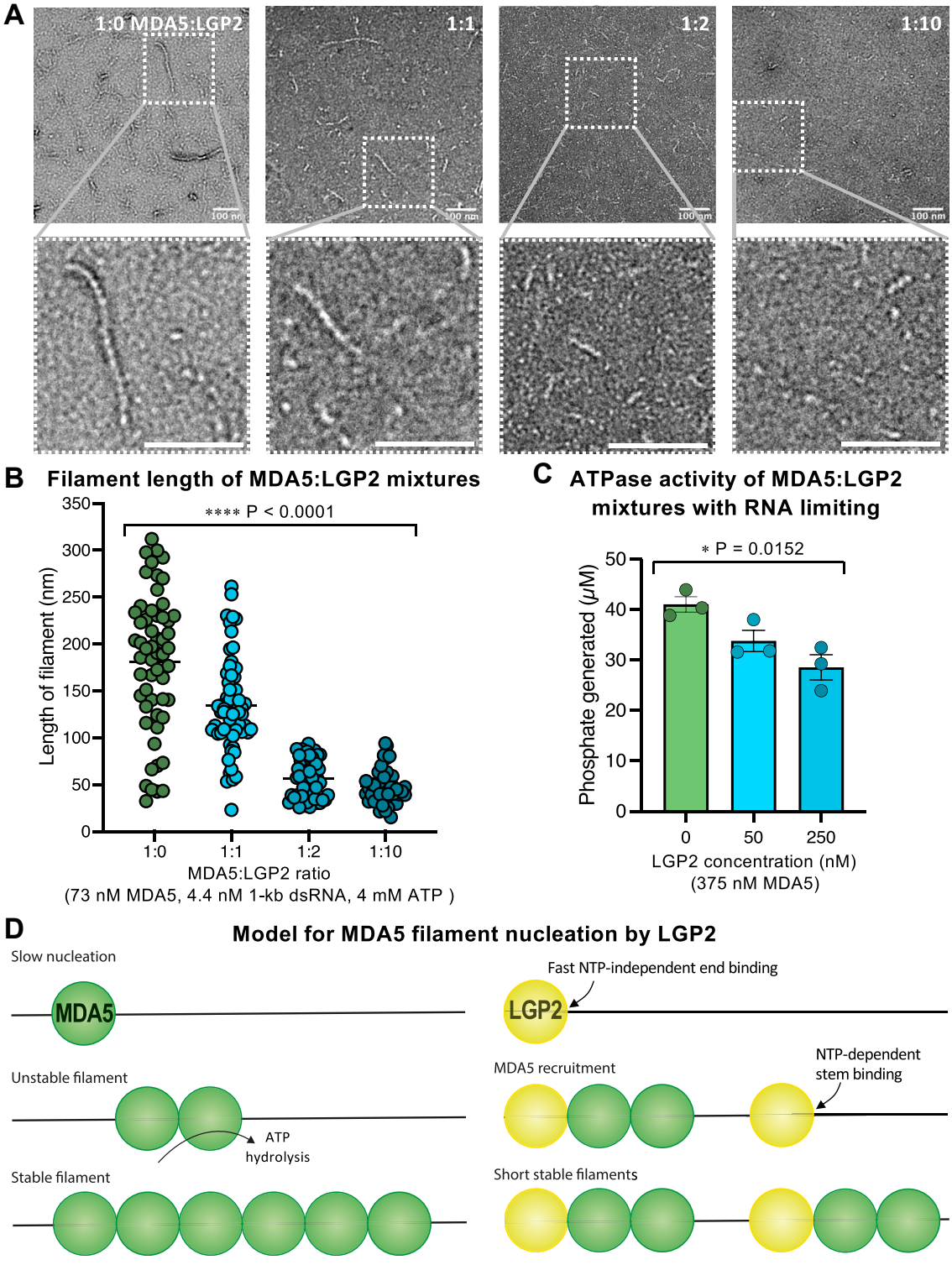

Figure 4. LGP2 promotes nucleation of MDA5 filament assembly at internal dsRNA sites. *A*, negative stain electron micrographs of filaments formed in the presence of 1-kb dsRNA, ATP, and different proportions of MDA5 and LGP2. The scale bars represent 100 nm. *B*, filament length measurements taken from electron micrographs including those shown in (*A*). Increasing amounts of LGP2 progressively reduced the average length of the resulting protein filaments. The number of measurements in each category from left to right was 56, 64, 53, and 48, respectively. *C*, ATPase activity of filaments formed in the presence of MDA5, LGP2, and 1-kb dsRNA with a substoichiometric number of 15-bp dsRNA binding sites. The concentration of 15-bp dsRNA binding sites was 313 nM. Data points are from three independent experiments. Error bars in (*B* and *C*) show the s.e.m.; statistical test: ordinary one-way ANOVA; see Supporting information for source data. *D*, proposed NTPase-dependent mechanism of MDA5 filament nucleation by LGP2 at internal dsRNA sites. MDA5, melanoma differentiation-associated protein 5.

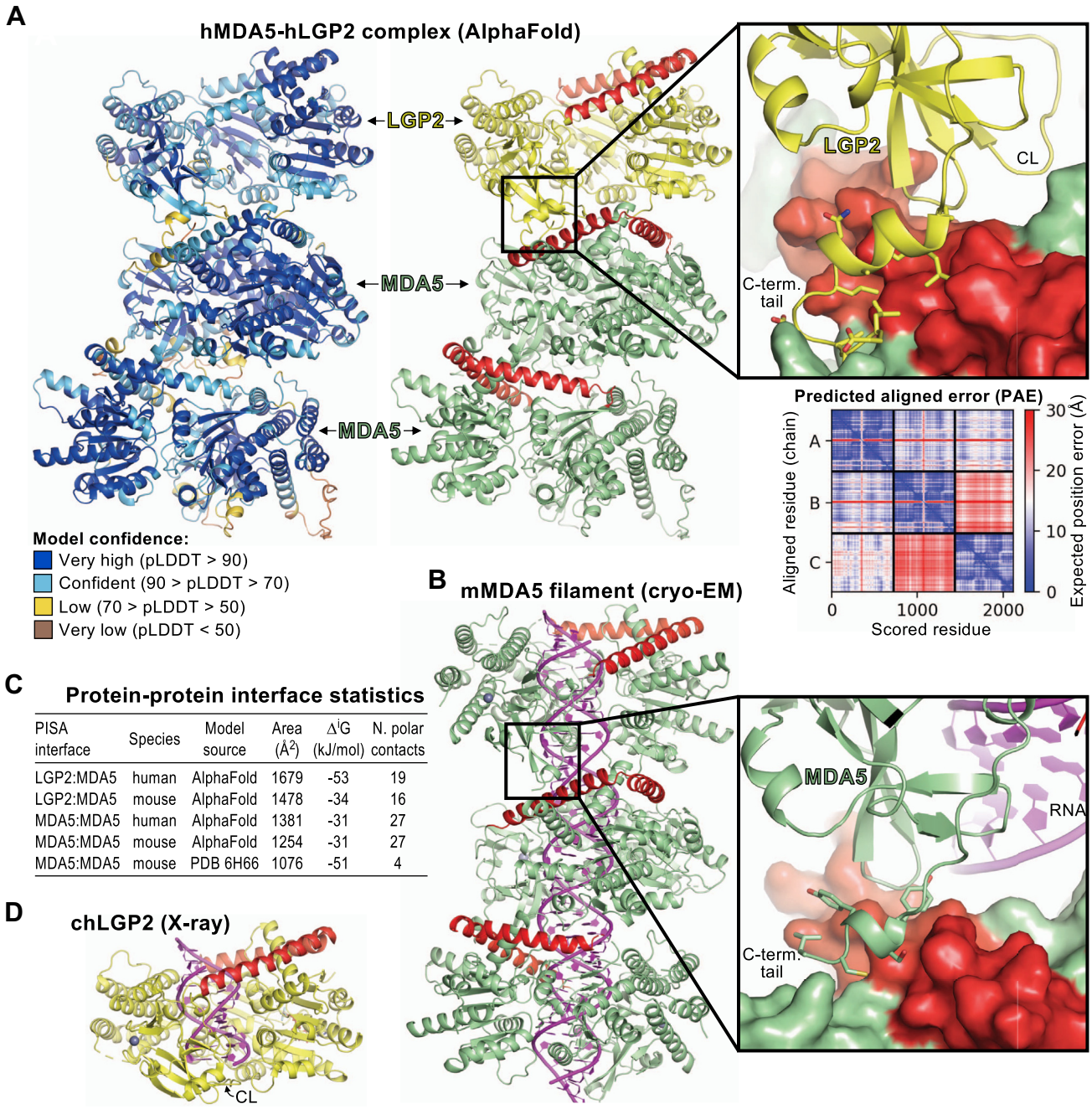

PISA interface	Species	Model source	Area (Å^2)	Δ^iG (kJ/mol)	N. polar contacts
LGP2:MDA5	human	AlphaFold	1679	-53	19
LGP2:MDA5	mouse	AlphaFold	1478	-34	16
MDA5:MDA5	human	AlphaFold	1381	-31	27
MDA5:MDA5	mouse	AlphaFold	1254	-31	27
MDA5:MDA5	mouse	PDB 6H66	1076	-51	4

Figure 5. Molecular modeling of MDA5-LGP2 complexes with AlphaFold-Multimer. *A*, AlphaFold model of a complex containing one LGP2 molecule and two MDA5 molecules colored by model confidence (pLDDT, according to the color code shown), *left*, and colored with MDA5 in *green*, LGP2 in *yellow*, and the pincer domains of MDA5 and LGP2 in *red*, *right*. The close-up shows the key contacts between LGP2 (*yellow*) and MDA5 (in surface representation). CL, capping loop. The predicted aligned error plot for this model is shown. *B*, cryo-EM structure of the MDA5-dsRNA filament without nucleotide and with 93° helical twist (PDB 6H66 (21)). This cryo-EM structure was selected because it lacks nucleotide and has similar helical twist to the AlphaFold models. The dsRNA is shown in *magenta*. The close-up shows contacts between adjacent MDA5 protomers at the region equivalent to that shown in the close-up in (A). *C*, protein-protein interface statistics from PISA (51) for MDA5 filaments and MDA5-LGP2 complexes modeled by AlphaFold (48–50). Statistics for the cryo-EM-derived MDA5 filament shown in (*B*) are shown for comparison. *D*, crystal structure of chicken LGP2 in complex with ADP-AlF$_4$-Mg and an end-bound 10-bp dsRNA (PDB 5JAJ (10)). CL, capping loop; PDB, Protein Data Bank; PISA, proteins, interfaces, structures, and assemblies. MDA5, melanoma differentiation-associated protein 5.

pincer domain facing away from the interface—is the opposite of what would have been expected if LGP2 nucleated MDA5 filaments from dsRNA ends. Indeed, to bind the free dsRNA end in an end-bound LGP2-dsRNA complex, MDA5 would need to form contacts with the LGP2 pincer domain, on the side opposite to the capping loop and C-terminal tail.

The C-terminal tail of LGP2 is required for ATP-dependent internal RNA binding

To test experimentally whether the LGP2 C-terminal tail interacts with MDA5 as predicted by the AlphaFold model we generated LGP2 truncation mutants with 8, 14, or 16 amino acids deleted from the C-terminal tail. As a reference, we also

generated LGP2 with the mutation K602A in the capping loop, which is near the C-terminal tail but does not form any direct contacts with MDA5 in the AlphaFold model. All four of these LGP2 mutants folded and had similar thermostabilities in differential scanning fluorimetry (Fig. S4). Ns-EM of 1:1 LGP2:MDA5 mixtures in the presence of 1-kb dsRNA and ATP showed that incubation of MDA5 with all three LGP2 C-terminal deletion mutants resulted in significantly longer filaments than with WT LGP2 or no LGP2 (Fig. 6). In contrast, addition of LGP2 K602A or WT LGP2 resulted in shorter filaments than with MDA5 (Figs. 4 and 6*A*). The increase in average filament length with the LGP2 C-terminal deletion mutants relative to WT LGP2 was ATP-dependent, as was the decrease in filament length with WT and K602A LGP2 relative to MDA5 alone. Indeed, in the absence of ATP none of the LGP2 mutants tested significantly altered the average filament length relative to WT LGP2 (Fig. 6*B*).

Having established above that LGP2 promotes ATP-dependent nucleation of MDA5 filament assembly from internal RNA sites (Fig. 4), the ATP-dependent effects of the LGP2 deletion mutants (Fig. 6*A*) imply that the C-terminal tail is required, directly or indirectly, for internal RNA binding of LGP2. Hence, deletion of the LGP2 C-terminal tail causes loss of internal RNA binding and results in longer MDA5 filaments (from fewer nucleation events) than with WT LGP2. The increase in filament length with the C-terminal deletion mutants beyond that of MDA5 alone (Fig. 6, *A* and *B*) is attributable to the end-binding activity of LGP2, which is independent of the C-terminal tail, allowing nucleation of MDA5 filaments and filament growth from the RNA ends. Consistent with this, the RNA binding affinity of LGP2 was not significantly altered by the C-terminal deletions in the absence of ATP (Fig. S2*B*). Moreover, in the structure of RNA end-bound LGP2 the C-terminal tail is facing away from the RNA and therefore unlikely to participate in recruitment of MDA5 (10). Together, the ATP-dependent effects of the five LGP2 variants tested on filament length provide experimental support for the AlphaFold model described above because the LGP2 C-terminal tail mediates most of the predicted interactions with MDA5 and the model is compatible with internal RNA binding, which is ATP-dependent, but not end-binding, which can occur in the absence of ATP.

Discussion

We have shown that adjacent MDA5 subunits in MDA5-dsRNA filaments hydrolyze ATP cooperatively. Since ATP hydrolysis promotes dissociation of MDA5 from suboptimal dsRNA ligands including endogenous RNA, cooperative ATP hydrolysis will trigger cooperative disassembly of MDA5 filaments form these ligands. Accordingly, the ATPase activity of mixtures of WT and ATPase-deficient MDA5 variants dropped exponentially as the amount of the ATPase-deficient variant was increased. Indeed, a 1:1 mixture of WT and ATPase-deficient MDA5 had only 20% of the ATPase activity of WT MDA5 (Fig. 1*A*). Mutations targeting the ATPase activity of MDA5 can therefore be expected to have a dominant negative effect on ATPase activity, and hence a dominant gain-of-function effect on MDA5-dependent interferon signaling activity. This provides a likely explanation for why ATPase-deficient MDA5 mutations are dominant autoinflammation alleles (2, 32, 33).

An additional consequence of cooperative ATP hydrolysis by MDA5 is to amplify the one base-pair RNA footprint expansion that accompanies each cycle of ATP hydrolysis by a single MDA5 molecule, allowing MDA5 filaments to displace bound viral or cellular proteins from the bound dsRNA. Our experiments with dsRNAs containing single-nucleotide bulges show that MDA5 filaments of 18 subunits or longer are required for maximal protein displacement activity. Conversely, interruptions of the RNA duplex every 250 bp are sufficient to impede protein displacement by MDA5 from both endogenous and viral RNAs. We note that a single A-to-I deamination by ADAR1 may have a similar effect on MDA5 protein displacement as a single-nucleotide bulge. In parallel, nucleation of MDA5-dsRNA filament formation by LGP2 reduces MDA5 filament length and hence the cooperativity of MDA5 ATP hydrolysis, which should in turn increase filament stability. These mechanisms confer protein displacement and filament repair activities independent of interferon signaling. Despite these activities, however, some virally encoded proteins cannot be displaced from RNA by MDA5, such as filovirus VP35 proteins, for example (52, 53).

A-to-I RNA editing by ADAR1 prevents MDA5 signaling from endogenous RNAs by weakening base-pairing in double-stranded segments (27, 28). In the absence of ADAR1 editing, endogenous dsRNAs trigger an MDA5-dependent interferon response that absolutely requires LGP2 (42). Cellular dsRNAs, such as inverted Alu repeats, are rarely longer than 150 bp and contain base-pair mismatches even without editing, making them poor ligands for MDA5. This suggests that LGP2, with its much lower nucleic acid selectivity, functions as an adaptor to nucleate MDA5 filament assembly on short or imperfect dsRNA ligands that would not otherwise support MDA5 signaling. LGP2 may have a similar adaptor or intercellular surveillance function in initiating MDA5 signaling from virus-derived dsRNA ligands that would not otherwise activate MDA5 signaling, thereby broadening the repertoire of viral RNAs sensed by the cell (54). Moreover, since LGP2 expression is stimulated by interferon (11), the surveillance function of LGP2 is expected to be enhanced following dsRNA recognition.

Our ATPase assays show that ATP hydrolysis modulates the RNA binding affinities of MDA5 and LGP2 in contrasting manners. Whereas ATP hydrolysis by MDA5 promotes dissociation from suboptimal dsRNA ligands, ATP hydrolysis by LGP2 promotes binding to internal sites on dsRNA, in the stem binding mode. In this respect, LGP2 is more similar to RIG-I in which ATP hydrolysis also promotes binding to internal dsRNA binding sites (36, 37). However, in contrast to RIG-I which reaches internal binding sites by local translocation from dsRNA ends (36, 37), our data show that LGP2 can bind directly to internal sites on dsRNA.

Although helicases from other groups within superfamily 2 hydrolyze all four types of NTPs (45, 46), the semiselective

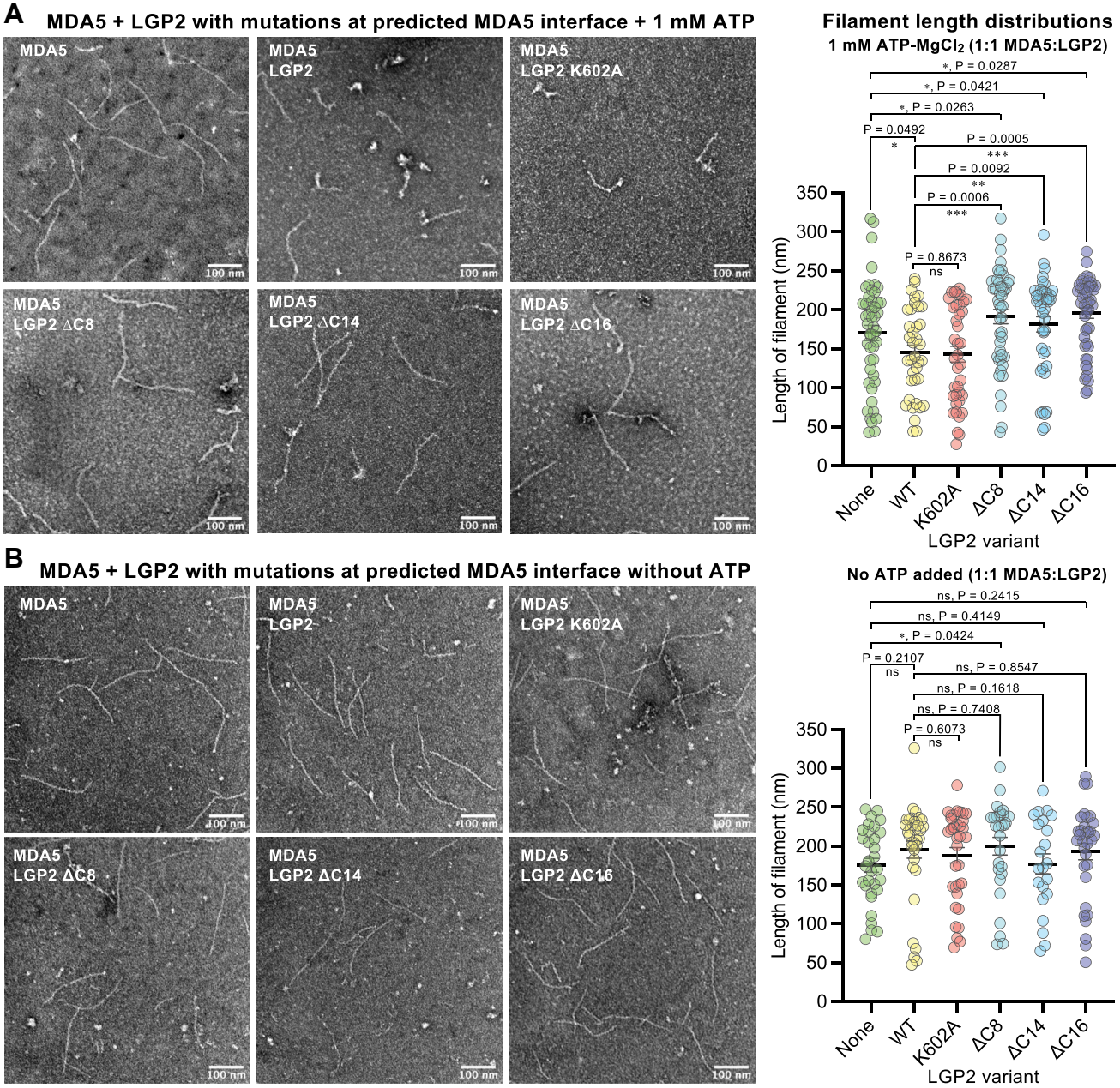

Figure 6. ATP-dependent effect of the LGP2 C-terminal tail on MDA5 filament assembly. *A*, left, negative stain electron micrographs of filaments formed in the presence of 4 mM ATP, 73 nM MDA5, and 4.4 nM 1-kb dsRNA, with or without 73 nM LGP2 (WT, K602A, ΔC8, ΔC14, or ΔC16). The scale bars represent 100 nm. *Right*, filament length measurements taken from electron micrographs including those shown on the *left*. The number of measurements for each sample type, from left to right, was 49, 37, 39, 46, 42, and 48. *B*, left, negative stain electron micrographs of filaments formed in the presence of 73 nM MDA5, and 4.4 nM 1-kb dsRNA, with or without 73 nM LGP2 (WT, K602A, ΔC8, ΔC14, or ΔC16). The scale bars represent 100 nm. *Right*, filament length measurements taken from electron micrographs including those shown on the *left*. The number of measurements for each sample type, from *left to right*, was 31, 35, 35, 28, 22, and 33. MDA5, melanoma differentiation-associated protein 5.

NTP hydrolysis of LGP2 distinguishes it from MDA5. We speculate that LGP2 may have evolved to broaden its nucleotide usage as a mechanism to maintain NTPase-dependent dsRNA binding, MDA5 filament nucleation, and hence interferon-β activation when ATP is depleted or when GTP or CTP is elevated in the cell. Many RNA viruses have different genomic nucleotide compositions than their hosts. Retroviruses genomes are A-rich, for example, and the rubella virus genome has exceptionally high GC content (70%) (47). Infection with these viruses will increase utilization of specific nucleotides—GTP and CTP in the case of rubella virus—which may become depleted or subject to increased turnover. Indeed, HIV, rubella virus and Epstein-Barr virus all induce host cells to increase expression of rate-limiting enzymes in the nucleotide biosynthesis pathway (55–57).

Our ATPase and electron microscopy data support the model that LGP2 utilizes its NTPase activity to bind to dsRNA at internal binding sites, from where it nucleates MDA5 filament assembly, consistent with previous evidence that LGP2 promotes MDA5 signaling and filament nucleation (39–41).

AlphaFold robustly predicts an MDA5-LGP2 interaction with LGP2 in an orientation that is incompatible with MDA5-LGP2 complex formation at dsRNA ends. The C-terminal tail of LGP2 mediates most of the contacts with MDA5 in the AlphaFold model. Although the position of the LGP2 C-terminal in the model suggests that it does not bind RNA directly (compare the close-ups in Fig. 5, *A* and *B*), it is required for ATP-dependent binding of LGP2 to internal RNA sites and the associated reduction in MDA5 filament length. Hence, our data suggest that LGP2 nucleates MDA5 filaments from internal sites on dsRNA as a stem binder in an ATP-dependent manner. However, LGP2 can bind to RNA ends and nucleate filament formation from the ends in the absence of NTPs. We therefore propose that internal stem binding as in the AlphaFold model and end binding as in the crystal structure both occur. We note that opposite molecular surfaces of LGP2 would interact with MDA5 in these stem- and end-binding modes, with the surface of LGP2 encompassing the C-terminal tail interacting with MDA5 only in the stem-binding mode.

We conclude that LGP2 promotes nucleation of MDA5 filaments at internal sites on dsRNA in an NTPase-dependent manner and at dsRNA ends in an NTPase-independent manner, resulting in shorter, more numerous filaments that are still capable of signaling. This work identifies novel molecular mechanisms contributing the selectivity and sensitivity of cytosolic dsRNA sensing by RIG-I-like receptors, with relevance to both healthy individuals and those with MDA5 mutations that result in autoinflammatory disease.

Experimental procedures

RNA and DNA reagents

RNAs were transcribed *in vitro* using the MEGAscript T7 Transcription Kit (Invitrogen, cat. no. AM1333) or HiScribe T7 High Yield RNA Synthesis Kit (New England BioLabs, cat. no. E2040S) following the manufacturers' protocols. The 40-bp ssRNA and 100-bp, 300-bp and 1-kb dsRNA (and ssRNA) contained the first 40, 100, 300, or 1000 bases of the mouse *IFIH1* gene, respectively. The complementary RNA strands were transcribed from DNA templates with a preceding 5′ TAATACGACTCACTATAG 3′ sequence. The *in vitro* transcription reactions were performed at 37 °C for 2, 4, 6 h, or overnight. Transcripts were treated with TURBO DNase and purified with the PureLink RNA Mini Kit (Thermo Fisher Scientific, cat. no. 12183018A) or the Monarch RNA Cleanup Kit (500 μg) (New England BioLabs, cat. no. T2050L). Samples were eluted in a nuclease-free duplex annealing buffer: 30 mM Hepes pH 7.5, 0.1 M KCl (Integrated DNA Technologies). Eluted transcripts were incubated at 95 °C for 5 min and cooled to room temperature over 2 h to eliminate secondary structure and enable annealing of complementary strands of RNA where necessary. A total of 1-kb dsRNA with three or six bulges was generated by hybridizing a 1-kb ssRNA sense strand with an antisense strand containing single guanosine nucleotides inserted internally every 250 bp or 143 bp throughout the sequence, respectively. See source data file (Fig. 1*F*) in Supporting information for RNA sequences.

To obtain internally biotinylated dsRNA, 10× Biotin RNA Labeling Mix (Roche, 11685597910), consisting of 10 mM each of ATP, CTP and GTP, 6.5 mM UTP and 3.5 mM Biotin-16-UTP, was added to the *in vitro* transcription reaction mix. 100 bp and 1-kb dsDNA was obtained by PCR amplification of the first 100 or 1000 bases of the mouse *IFIH1* gene. DNA:RNA hybrids were produced using *in vitro* transcribed ssRNA to generate and hybridize the complementary DNA with the RevertAid H Minus Reverse Transcriptase kit (Thermo Fisher Scientific, cat. no. EP045). Some samples were incubated with RNase H (New England BioLabs, cat. no. M0297S), DNA:RNA hybrid-specific nuclease, for 30 min at 37 °C (Fig. 3*A*). High molecular weight poly(I:C) RNA was purchased from InvivoGen (cat. no. tlrl-pic). 4-kb linear dsRNA was a gift from David Dulin (VU University Amsterdam). The ssRNAs with complex secondary structure (ssRNA1-3) were gifts from Irene Díaz-López from the laboratory of Venki Ramakrishnan (MRC Laboratory of Molecular Biology). See source data file (Fig. S3) in Supporting information for RNA sequences.

Expression and purification of MDA5

A gene encoding murine MDA5 (*Ifih1*, UniProt: Q8R5F7) was cloned into the pET28a vector with an N-terminal hexahistidine tag followed by a tobacco etch virus (TEV) protease cleavage site as described (18). MDA5 residues 646 to 663, in the flexible L2 surface loop of the helicase 2 insert domain (Hel2i), were deleted for solubility, resulting in a 114-kDa polypeptide chain. This ΔL2 loop deletion does not affect the dsRNA binding, ATPase or interferon signaling activities of MDA5 (18, 20, 21). Expression plasmids for MDA5 mutants were generated by site-directed mutagenesis.

Escherichia coli Rosetta2(DE3)pLysS cells (Novagen, cat. no. 71403) were transformed with pET28a-MDA5ΔL2-His_6 and grown in 2xTY medium to A_{600} 0.4 to 0.6 at 37 °C. After cooling to 17 °C, protein expression was induced with 0.5 mM IPTG overnight at 17 °C. Harvested cells were resuspended in 30 mM Hepes pH 7.7, 0.15 M NaCl, 5% glycerol, 1 mM Tris(2-carboxyethyl)phosphine (TCEP), cOmplete, EDTA-free Protease Inhibitor Cocktail (Roche, cat. no. 11873580001) and Benzonase Nuclease (Merck, cat. no. 70746), then lysed by ultrasonication on ice. The lysate was centrifuged at 37,500*g* for 1 h. The supernatant was loaded onto a preequilibrated 5 ml HisTrap HP column (Cytiva, cat. no. 17–5248–02), washed with 30 mM Hepes pH 7.7, 0.5 M NaCl, 20 mM imidazole and 1 mM TCEP, and MDA5 was eluted with 30 mM Hepes 7.5, 0.15 M NaCl, 5% glycerol, 0.3 M imidazole, and 1 mM TCEP. MDA5 was further purified on a Resource Q anion exchange column (Cytiva) (buffer A: 20 mM Hepes 7.5, 0.1 M NaCl, 2 mM DTT; buffer B: 20 mM Hepes 7.5, 1 M NaCl, 2 mM DTT), and a Superdex 200 Increase 10/300 Gl size-exclusion column (Cytiva) in 20 mM Hepes pH 7.8,

0.15 M KCl, 1 mM DTT, and 5% glycerol. Purified protein was flash-frozen and stored at −80 °C.

Expression and purification of LGP2

A gene encoding murine LGP2 (*Dhx58*, UniProt: Q99J87) was cloned into the pACEBAC1 baculovirus transfer vector with an N-terminal 2x-Strep tag followed by TEV protease cleavage site. The K30G, R32G, and K602A, and C-terminal tail truncation (ΔC8, ΔC14, and ΔC16) mutants were introduced into the LGP2 construct by site-directed mutagenesis.

The pACEBAC1-2xStrepTEV-LGP2 plasmids were transformed into *E. coli* DH10Bac cells. Purified bacmid DNA was transfected into Sf9 insect cells (Invitrogen) to produce secreted recombinant baculovirus. For LGP2 expression, Sf9 cells were infected at a density of 3×10^6 cells/ml with 0.5% (v/v) of third passage (P3) baculovirus stock and incubated at 27 °C. The cells were harvested 60 to 72 h post infection. The cells were lysed with a chilled Dounce homogenizer in 30 mM Hepes, pH 7, 0.3 M NaCl, 1 mM TCEP, 5% glycerol supplemented with EDTA-free Complete Protease Inhibitor (Roche), and Salt-Active Nuclease (Sigma-Aldrich, cat. no. SRE0015). The lysate was clarified by centrifugation. The lysate supernatant was incubated on a nutator at 4 °C for 2 to 3 h with 1 ml of Strep-Tactin Sepharose resin (IBA-Lifesciences, cat. no. 2–1201–025) equilibrated in 30 mM Hepes, pH 7, 0.15 M NaCl, 1 mM TCEP, 5% glycerol, and EDTA-free Complete Protease Inhibitor (Roche). The protein was eluted with 2.5 mM d-desthiobiotin pH 8. The eluate was further purified on a Superdex 200 Increase 10/300 Gl size-exclusion column in 25 mM Hepes pH 7.7, 0.15 KCl, 1 mM TCEP.

Negative stain electron microscopy

Carbon film in 300-mesh grids (Agar Scientific) were glow discharged at 25 mA for 1 min. Samples were applied to the grids and washed with RNase-free water before staining with 2% (w/v) uranyl acetate. To visualize MDA5 filaments from the cooperativity assays, protein was incubated on ice for 30 min with 10 mM ATPγS with a final concentration of 200 nM MDA5 and 10 nM 1-kb dsRNA. To visualize LGP2-MDA5 complex formation, 73 nM MDA5 and 73, 146, or 730 nM LGP2 were incubated with 4 mM ATP and 4.4 nM 1-kb dsRNA on ice for 30 min. Samples containing MDA5 and 73, 146, and 730 nM LGP2 were rapidly diluted 1:2, 1:3, and 1:10 fold, respectively, before staining. All ns-EM images were collected on a 120 kV Tecnai G2 Spirit TEM (Thermo Fisher Scientific). Images were collected at −2 to −4 μm defocus, 26000× magnification, and 4 Å per pixel. Results were analyzed and filament length quantified with ImageJ (v1.5, imagej.net).

ATPase assays

ATPase activities were measured with the ATPase/GTPase Activity Assay Kit (Sigma-Aldrich, cat. no. MAK113) based on the colorimetric change of malachite green in the presence of inorganic phosphate produced by ATP hydrolysis. Reactions in clear, flat-bottom 96-well plates were read using a CLARIOstar microplate reader (BMG LABTECH) at 620 nm. Reactions contained 180 nM protein, 25 ng nucleic acid, 4 mM ATP, and 4 mM $MgSO_4$ unless stated otherwise. Reactions were incubated at 37 °C for 3 min and quenched with EDTA. For the cooperativity assays, WT and ATPase-deficient variants were mixed at various molar ratios while maintaining the same total protein concentration of 200 nM. The WT:mutant mixtures were incubated with 1.25 nM 1-kb dsRNA at 37 °C for 3 min. Results were analyzed with Prism v9.5.1 (GraphPad, graphpad.com).

Biotin-streptavidin displacement assay

Biotinylated RNA duplexes were generated by incorporation of Biotin-16-UTP (Sigma-Aldrich) during *in vitro* transcription of 1-kb sense and antisense RNA strands, or 1-kb sense and 1003- or 1006-bp antisense strands for the 3- and 6-bulge RNA duplexes, respectively (see above for *in vitro* transcription protocol). Ratios of incorporation were calculated to synthesize RNA duplexes with an average of 2 to 8 conjugated biotins. A total of 2 μg/μl biotinylated dsRNA and unlabeled control were incubated with 55 mM streptavidin (Thermo Fisher Scientific, cat. no. 211122) dissolved in nuclease-free water with 20 mM potassium phosphate pH 6.5. This mixture was incubated with 350 nM mMDA5, 245 mM biotin (Sigma-Aldrich, B4501; from a stock solution in 0.5% dimethyl sulfoxide and diethyl pyrocarbonate-treated water) and 10 mM ATP-$MgSO_4$ for 30 min at 37 °C. Streptavidin displacement was visualized by gel electrophoresis on 1% agarose or 4 to 20% Tris/Borate/EDTA polyacrylamide gels stained with SYBR Gold Nucleic Acid Gel Stain (Thermo Fisher Scientific, cat. no. S11494). The reactions were incubated at 65 °C for 5 min in 0.5 M potassium phosphate pH 7.4, 0.5 M NaCl, 6% SDS, and 1× SDS Gel Loading Dye (New England BioLabs, cat. no. B7024S)—this treatment displaced MDA5 and LGP2 but not streptavidin from biotinylated RNA. The samples were loaded on the gels and the gels were run in Tris/Borate/EDTA buffer at 200 V and 4 °C. Gels were stained with DNA stain at room temperature for 2 h. Gels were imaged in a G:BOX imaging system and GeneSys v1.5 (Syngene, syngene.com/software/genesys-rapid-gel-image-capture).

BLI protein-RNA binding assays

Pierce RNA 3′ End Biotinylation Kit (Thermo Fisher Scientific, cat. no. 20160) was used to label the 3' end of 1-kb RNA duplexes (produced as described above) with biotin. The 3′-biotinylated RNA was immobilized on an Octet streptavidin (SA) Biosensor (Sartorius). Three micrograms of biotinylated RNA were incubated per sensor for 300 s. MDA5 and LGP2 were added, individually or together, at 0.1 μm or 1 μM. The optical interference pattern of white light was used to measure binding kinetics with the Octet BLI Label-Free Detection System (Sartorius). MDA5 and LGP2 dissociation was measured by flowing buffer (20 mM Hepes pH 7.4, 0.15 M KCl, and 1 mM TCEP) over the sensor. BLI kinetic data were analyzed with Octet Analysis Studio (Sartorius) to determine dissociation constants (K_d). K_d values were calculated from the association rate.

Electrophoretic mobility shift assays

Mixtures containing 100 ng nucleic acid and 1 μM MDA5 or LGP2 were incubated for 15 min at 4 °C in 20 mM Hepes pH 7.4, 0.15 M KCl, and 1 mM TCEP. After addition of NativePAGE Sample Buffer (Thermo Fisher Scientific, cat. no. BN2003), samples were loaded onto a 4 to 20% polyacrylamide gel and run in in Tris-borate buffer (0.1 M Tris, 0.1 M boric acid, pH 8.3) for 90 min at 200 V at 4 °C. Gels were stained with SYBR Gold Nucleic Acid Gel Stain (Thermo Fisher Scientific, cat. no. S11494) and imaged in a G:BOX imaging system and GeneSys v1.5 (Syngene, syngene.com/software/genesys-rapid-gel-image-capture).

AlphaFold2 modeling

Atomic models of MDA5-LGP2 complexes were predicted with a local installation of AlphaFold2-v2.3.1 (48, 49) (deepmind.google/technologies/alphafold) using multimer mode as implemented by ColabFold v1.5.2 (50) (colab.research.google.com/github/sokrypton/ColabFold/blob/main/AlphaFold2.ipynb) with the use of MMseqs2 for multiple sequence alignment (MSA). The amino acid sequences of human or mouse LGP2 (all residues) and MDA5-ΔCARD (residues 306–1025) were used as the input. Polypeptide geometry in the models was regularized by post-prediction relaxation using the Amber force field. The maximum number of recycles was set to 20. No MSA cutoff was used. The sequence pairing mode was set to pair sequences from the same species and unpaired MSA. The multimer model was set to multimer-v3. Use of available template files from the Protein Data Bank had no significant effect on atomic model prediction. Five atomic models were output from each AlphaFold run. Protein interfaces were analyzed with the protein interfaces, surfaces, and assemblies (PISA) service at the European Bioinformatics Institute [http://www.ebi.ac.uk/pdbe/prot_int/pistart.html] (51). Atomic coordinates of a model generated by AlphaFold-Multimer containing two human MDA5 molecules and one human LGP2 molecule are available at ModelArchive (https://doi.org/10.5452/ma-c6y1h).

Differential scanning fluorimetry

Ten microliter samples of 25 μM LGP2 in 20 mM Hepes pH 7.4, 0.15 M KCl, and 1 mM TCEP were loaded into glass capillaries (NanoTemper) by capillary action. Intrinsic protein fluorescence at 330 nm and 350 nm, F330 and F350, respectively, was measured from 15 °C to 95 °C with a ramp rate of 2 °C per minute with a Prometheus NT.48 nano-fluorimeter (NanoTemper). The melting temperatures were calculated with the PR.Stability Analysis software (NanoTemper, nanotempertech.com/prometheus/nt48-software) as the temperature at the peak of the first derivative of F350:F330 *versus* temperature (Fig. S4).

Statistics

No statistical methods were used to predetermine sample size, experiments were not randomized, and the investigators were not blinded to experimental outcomes. ATPase assays were performed at least three times in independent experiments. Scatter plots, histograms, and error bars were plotted with GraphPad Prism 9.5.1 and Microsoft Excel v.16.72 (microsoft.com/microsoft-365). Statistical significance was assessed using paired or unpaired two-tailed t-tests (assuming Gaussian distributions, without Welch's correction), or a one-way ANOVA with Prism 9. Paired t-tests were used for comparing pairs of samples except if fewer than three pairs were available, when unpaired two-tailed t-tests were used. A one-way ANOVA was used to assess the statistical significance of differences in the means of a continuous variable across multiple groups, such as the mean length or ATPase activity of MDA5 filaments with different amounts of LGP2 added (Figs. 4, *B* and *C* and 6, *A* and *B*). Statistical significance was assigned as follows: n.s., $p > 0.05$; $^{*}p < 0.05$; $^{**}p < 0.01$; $^{***}p < 0.001$.

Data availability

The AlphaFold model is available in ModelArchive (modelarchive.org) with accession code ma-c6y1h at https://dx.doi.org/10.5452/ma-c6y1h. The other data underlying this article are available in the article and in its online supporting information.

Supporting information—This article contains supporting information.

Acknowledgments—We thank Giuseppe Cannone and Grigory Sharov (MRC-LMB EM Facility) for assistance in EM data collection. We thank Stephen McLaughlin and Chris Batters (MRC-LMB Biophysics Facility) for assistance with Octet experiments. We thank Irene Díaz-López (MRC-LMB) for providing the ssRNAs with complex secondary structure. We thank Salina Quack and David Dulin (VU University Amsterdam) for providing the linear dsRNA. We thank Frank Adolf (University of Cambridge) for his advice on baculovirus expression. We thank members of the Modis lab for insightful discussions. We thank MRC-LMB Scientific Computing for computing support and Sami Chaaban (MRC-LMB) for cluster maintenance of ColabFold. We would like to acknowledge the support of the MRC-LMB Media & Glass Wash facility. We thank Jianguo Shi (MRC-LMB Baculovirus Facility) for assistance with insect cell culture.

Author contributions—R. S., Y. W., A. H. d. V., K. E. L., S. M., M. T. K. C., and Y. M. investigation; R. S., Y. W., A. H. d. V., K. E. L., B. J. F., and Y. M. methodology; R. S., Y. W., A. H. d. V., and Y. M. visualization; R. S. and Y. M. conceptualization; R. S., A. H. d. V., B. J. F., and Y. M. funding acquisition; R. S., K. E. L., B. J. F., and Y. M. writing–review and editing; B. J. F., and Y. M. supervision; B. J. F., and Y. M. project administration; Y. M. formal analysis; Y. M. writing–original draft.

Funding and additional information—This work was supported by the Wellcome Trust [101908/Z/13/Z to Y. M., 217191/Z/19/Z to Y. M., 215378/Z/19/Z to R. S.]; and the Human Frontier Science Program [LT000454/2021-L to A. H. d. V.]. Funding for open access charge: University of Cambridge.

Conflict of interest—Y. M. is a consultant for Related Sciences LLC and has profits interests in Danger Bio LLC. B. J. F. is an Editorial Board Member for the Journal of Biological Chemistry and was not

involved in the editorial review or the decision to publish this article. None of the other authors have any conflicts of interest with the contents of this article.

Abbreviations—The abbreviations used are: ADAR1, adenosine deaminase RNA-specific; BLI, bio-layer interferometry; CARD, caspase recruitment domain; CTD, C-terminal domain; MDA5, melanoma differentiation-associated protein 5; MSA, multiple sequence alignment; ns-EM, negative-stain electron microscopy; TCEP, Tris(2-carboxyethyl)phosphine; TEV, tobacco etch virus.

References

1. Hur, S. (2019) Double-stranded RNA sensors and modulators in innate immunity. *Annu. Rev. Immunol.* **37**, 349–375
2. Rodero, M. P., and Crow, Y. J. (2016) Type I interferon-mediated monogenic autoinflammation: the type I interferonopathies, a conceptual overview. *J. Exp. Med.* **213**, 2527–2538
3. Kato, H., Sato, S., Yoneyama, M., Yamamoto, M., Uematsu, S., Matsui, K., *et al.* (2005) Cell type-specific involvement of RIG-I in antiviral response. *Immunity* **23**, 19–28
4. Yoneyama, M., Kikuchi, M., Matsumoto, K., Imaizumi, T., Miyagishi, M., Taira, K., *et al.* (2005) Shared and unique functions of the DExD/H-box helicases RIG-I, MDA5, and LGP2 in antiviral innate immunity. *J. Immunol.* **175**, 2851–2858
5. Kato, H., Takeuchi, O., Sato, S., Yoneyama, M., Yamamoto, M., Matsui, K., *et al.* (2006) Differential roles of MDA5 and RIG-I helicases in the recognition of RNA viruses. *Nature* **441**, 101–105
6. Kato, H., Takeuchi, O., Mikamo-Satoh, E., Hirai, R., Kawai, T., Matsushita, K., *et al.* (2008) Length-dependent recognition of double-stranded ribonucleic acids by retinoic acid-inducible gene-I and melanoma differentiation-associated gene 5. *J. Exp. Med.* **205**, 1601–1610
7. Venkataraman, T., Valdes, M., Elsby, R., Kakuta, S., Caceres, G., Saijo, S., *et al.* (2007) Loss of DExD/H box RNA helicase LGP2 manifests disparate antiviral responses. *J. Immunol.* **178**, 6444–6455
8. Pippig, D. A., Hellmuth, J. C., Cui, S., Kirchhofer, A., Lammens, K., Lammens, A., *et al.* (2009) The regulatory domain of the RIG-I family ATPase LGP2 senses double-stranded RNA. *Nucleic Acids Res.* **37**, 2014–2025
9. Li, X., Ranjith-Kumar, C. T., Brooks, M. T., Dharmaiah, S., Herr, A. B., Kao, C., *et al.* (2009) The RIG-I-like receptor LGP2 recognizes the termini of double-stranded RNA. *J. Biol. Chem.* **284**, 13881–13891
10. Uchikawa, E., Lethier, M., Malet, H., Brunel, J., Gerlier, D., and Cusack, S. (2016) Structural Analysis of dsRNA binding to anti-viral pattern recognition receptors LGP2 and MDA5. *Mol. Cell* **62**, 586–602
11. Satoh, T., Kato, H., Kumagai, Y., Yoneyama, M., Sato, S., Matsushita, K., *et al.* (2010) LGP2 is a positive regulator of RIG-I- and MDA5-mediated antiviral responses. *Proc. Natl. Acad. Sci. U. S. A.* **107**, 1512–1517
12. Kumar, A., Haque, J., Lacoste, J., Hiscott, J., and Williams, B. R. (1994) Double-stranded RNA-dependent protein kinase activates transcription factor NF-kappa B by phosphorylating I kappa B. *Proc. Natl. Acad. Sci. U. S. A.* **91**, 6288–6292
13. Vijay-Kumar, M., Gentsch, J. R., Kaiser, W. J., Borregaard, N., Offermann, M. K., Neish, A. S., *et al.* (2005) Protein kinase R mediates intestinal epithelial gene remodeling in response to double-stranded RNA and live rotavirus. *J. Immunol.* **174**, 6322–6331
14. Chebath, J., Benech, P., Revel, M., and Vigneron, M. (1987) Constitutive expression of (2'-5') oligo A synthetase confers resistance to picornavirus infection. *Nature* **330**, 587–588
15. Kristiansen, H., Scherer, C. A., McVean, M., Iadonato, S. P., Vends, S., Thavachelvam, K., *et al.* (2010) Extracellular 2'-5' oligoadenylate synthetase stimulates RNase L-independent antiviral activity: a novel mechanism of virus-induced innate immunity. *J. Virol.* **84**, 11898–11904
16. Bauernfried, S., Scherr, M. J., Pichlmair, A., Duderstadt, K. E., and Hornung, V. (2021) Human NLRP1 is a sensor for double-stranded RNA. *Science* **371**, eabd0811
17. Peisley, A., Lin, C., Wu, B., Orme-Johnson, M., Liu, M., Walz, T., *et al.* (2011) Cooperative assembly and dynamic disassembly of MDA5 filaments for viral dsRNA recognition. *Proc. Natl. Acad. Sci. U. S. A.* **108**, 21010–21015
18. Berke, I. C., and Modis, Y. (2012) MDA5 cooperatively forms dimers and ATP-sensitive filaments upon binding double-stranded RNA. *EMBO J.* **31**, 1714–1726
19. Berke, I. C., Yu, X., Modis, Y., and Egelman, E. H. (2012) MDA5 assembles into a polar helical filament on double-stranded RNA. *Proc. Natl. Acad. Sci. U. S. A.* **109**, 18437–18441
20. Wu, B., Peisley, A., Richards, C., Yao, H., Zeng, X., Lin, C., *et al.* (2013) Structural basis for dsRNA recognition, filament formation, and antiviral signal activation by MDA5. *Cell* **152**, 276–289
21. Yu, Q., Qu, K., and Modis, Y. (2018) Cryo-EM structures of MDA5-dsRNA filaments at different stages of ATP hydrolysis. *Mol. Cell* **72**, 999–1012.e6
22. Yu, Q., Herrero Del Valle, A., Singh, R., and Modis, Y. (2021) MDA5 disease variant M854K prevents ATP-dependent structural discrimination of viral and cellular RNA. *Nat. Commun.* **12**, 6668
23. Hou, F., Sun, L., Zheng, H., Skaug, B., Jiang, Q. X., and Chen, Z. J. (2011) MAVS forms functional prion-like aggregates to activate and propagate antiviral innate immune response. *Cell* **146**, 448–461
24. Wu, B., Peisley, A., Tetrault, D., Li, Z., Egelman, E. H., Magor, K. E., *et al.* (2014) Molecular imprinting as a signal-activation mechanism of the viral RNA sensor RIG-I. *Mol. Cell* **55**, 511–523
25. Yin, X., Riva, L., Pu, Y., Martin-Sancho, L., Kanamune, J., Yamamoto, Y., *et al.* (2021) MDA5 governs the innate immune response to SARS-CoV-2 in lung epithelial cells. *Cell Rep.* **34**, 108628
26. Rebendenne, A., Valadao, A. L. C., Tauziet, M., Maarifi, G., Bonaventure, B., McKellar, J., *et al.* (2021) SARS-CoV-2 triggers an MDA-5-dependent interferon response which is unable to control replication in lung epithelial cells. *J. Virol.* **95**, e02415–e02420
27. Ahmad, S., Mu, X., Yang, F., Greenwald, E., Park, J. W., Jacob, E., *et al.* (2018) Breaching self-tolerance to Alu duplex RNA underlies MDA5-mediated inflammation. *Cell* **172**, 797–810.e13
28. Chung, H., Calis, J. J. A., Wu, X., Sun, T., Yu, Y., Sarbanes, S. L., *et al.* (2018) Human ADAR1 prevents endogenous RNA from triggering translational shutdown. *Cell* **172**, 811–824.e14
29. Mehdipour, P., Marhon, S. A., Ettayebi, I., Chakravarthy, A., Hosseini, A., Wang, Y., *et al.* (2020) Epigenetic therapy induces transcription of inverted SINEs and ADAR1 dependency. *Nature* **588**, 169–173
30. Tunbak, H., Enriquez-Gasca, R., Tie, C. H. C., Gould, P. A., Mlcochova, P., Gupta, R. K., *et al.* (2020) The HUSH complex is a gatekeeper of type I interferon through epigenetic regulation of LINE-1s. *Nat. Commun.* **11**, 5387
31. Rutsch, F., MacDougall, M., Lu, C., Buers, I., Mamaeva, O., Nitschke, Y., *et al.* (2015) A specific IFIH1 gain-of-function mutation causes Singleton-Merten syndrome. *Am. J. Hum. Genet.* **96**, 275–282
32. Rice, G. I., Del Toro Duany, Y., Jenkinson, E. M., Forte, G. M., Anderson, B. H., Ariaudo, G., *et al.* (2014) Gain-of-function mutations in IFIH1 cause a spectrum of human disease phenotypes associated with upregulated type I interferon signaling. *Nat. Genet.* **46**, 503–509
33. Rice, G. I., Park, S., Gavazzi, F., Adang, L. A., Ayuk, L. A., Van Eyck, L., *et al.* (2020) Genetic and phenotypic spectrum associated with IFIH1 gain-of-function. *Hum. Mutat.* **41**, 837–849
34. Peisley, A., Jo, M. H., Lin, C., Wu, B., Orme-Johnson, M., Walz, T., *et al.* (2012) Kinetic mechanism for viral dsRNA length discrimination by MDA5 filaments. *Proc. Natl. Acad. Sci. U. S. A.* **109**, E3340–E3349
35. Yao, H., Dittmann, M., Peisley, A., Hoffmann, H. H., Gilmore, R. H., Schmidt, T., *et al.* (2015) ATP-dependent effector-like functions of RIG-I-like receptors. *Mol. Cell* **58**, 541–548
36. Devarkar, S. C., Schweibenz, B., Wang, C., Marcotrigiano, J., and Patel, S. S. (2018) RIG-I uses an ATPase-powered translocation-throttling mechanism for kinetic proofreading of RNAs and oligomerization. *Mol. Cell* **72**, 355–368.e4
37. Myong, S., Cui, S., Cornish, P. V., Kirchhofer, A., Gack, M. U., Jung, J. U., *et al.* (2009) Cytosolic viral sensor RIG-I is a 5'-triphosphate-dependent translocase on double-stranded RNA. *Science* **323**, 1070–1074

38. Childs, K. S., Randall, R. E., and Goodbourn, S. (2013) LGP2 plays a critical role in sensitizing mda-5 to activation by double-stranded RNA. *PLoS One* **8**, e64202
39. Bruns, A. M., Pollpeter, D., Hadizadeh, N., Myong, S., Marko, J. F., and Horvath, C. M. (2013) ATP hydrolysis enhances RNA recognition and antiviral signal transduction by the innate immune sensor, laboratory of genetics and physiology 2 (LGP2). *J. Biol. Chem.* **288**, 938–946
40. Bruns, A. M., Leser, G. P., Lamb, R. A., and Horvath, C. M. (2014) The innate immune sensor LGP2 activates antiviral signaling by regulating MDA5-RNA interaction and filament assembly. *Mol. Cell* **55**, 771–781
41. Duic, I., Tadakuma, H., Harada, Y., Yamaue, R., Deguchi, K., Suzuki, Y., *et al.* (2020) Viral RNA recognition by LGP2 and MDA5, and activation of signaling through step-by-step conformational changes. *Nucleic Acids Res.* **48**, 11664–11674
42. Stok, J. E., Oosenbrug, T., Ter Haar, L. R., Gravekamp, D., Bromley, C. P., Zelenay, S., *et al.* (2022) RNA sensing *via* the RIG-I-like receptor LGP2 is essential for the induction of a type I IFN response in ADAR1 deficiency. *EMBO J.* **41**, e109760
43. Massey, T. H., Mercogliano, C. P., Yates, J., Sherratt, D. J., and Lowe, J. (2006) Double-stranded DNA translocation: structure and mechanism of hexameric FtsK. *Mol. Cell* **23**, 457–469
44. Shin, J. H. (2008) Helicase translocation assay method using avidin and biotinylated nucleotides. *Biotechnol. Lett.* **30**, 2007–2012
45. Robert-Paganin, J., Halladjian, M., Blaud, M., Lebaron, S., Delbos, L., Chardon, F., *et al.* (2017) Functional link between DEAH/RHA helicase Prp43 activation and ATP base binding. *Nucleic Acids Res.* **45**, 1539–1552
46. Fairman-Williams, M. E., Guenther, U. P., and Jankowsky, E. (2010) SF1 and SF2 helicases: family matters. *Curr. Opin. Struct. Biol.* **20**, 313–324
47. Phakaratsakul, S., Sirihongthong, T., Boonarkart, C., Suptawiwat, O., and Auewarakul, P. (2018) Genome polarity of RNA viruses reflects the different evolutionary pressures shaping codon usage. *Arch. Virol.* **163**, 2883–2888
48. [preprint] Evans, R., O'Neill, M., Pritzel, A., Antropova, N., Senior, A., Green, T., *et al.* (2021) Protein complex prediction with AlphaFold-Multimer. *bioRxiv*. https://doi.org/10.1101/2021.10.04.463034
49. Jumper, J., Evans, R., Pritzel, A., Green, T., Figurnov, M., Ronneberger, O., *et al.* (2021) Highly accurate protein structure prediction with AlphaFold. *Nature* **596**, 583–589
50. Mirdita, M., Schutze, K., Moriwaki, Y., Heo, L., Ovchinnikov, S., and Steinegger, M. (2022) ColabFold: making protein folding accessible to all. *Nat. Methods* **19**, 679–682
51. Krissinel, E., and Henrick, K. (2007) Inference of macromolecular assemblies from crystalline state. *J. Mol. Biol.* **372**, 774–797
52. Ramanan, P., Edwards, M. R., Shabman, R. S., Leung, D. W., Endlich-Frazier, A. C., Borek, D. M., *et al.* (2012) Structural basis for Marburg virus VP35-mediated immune evasion mechanisms. *Proc. Natl. Acad. Sci. U. S. A.* **109**, 20661–20666
53. Leung, D. W., Prins, K. C., Borek, D. M., Farahbakhsh, M., Tufariello, J. M., Ramanan, P., *et al.* (2010) Structural basis for dsRNA recognition and interferon antagonism by Ebola VP35. *Nat. Struct. Mol. Biol.* **17**, 165–172
54. Deddouche, S., Goubau, D., Rehwinkel, J., Chakravarty, P., Begum, S., Maillard, P. V., *et al.* (2014) Identification of an LGP2-associated MDA5 agonist in picornavirus-infected cells. *Elife* **3**, e01535
55. Bilz, N. C., Jahn, K., Lorenz, M., Ludtke, A., Hubschen, J. M., Geyer, H., *et al.* (2018) Rubella viruses shift cellular bioenergetics to a more oxidative and glycolytic phenotype with a strain-specific requirement for glutamine. *J. Virol.* **92**, e00934-18
56. Hegedus, A., Kavanagh Williamson, M., Khan, M. B., Dias Zeidler, J., Da Poian, A. T., El-Bacha, T., *et al.* (2017) Evidence for altered glutamine metabolism in human immunodeficiency virus type 1 infected primary human CD4(+) T cells. *AIDS Res. Hum. Retroviruses* **33**, 1236–1247
57. Liang, J. H., Wang, C., Yiu, S. P. T., Zhao, B., Guo, R., and Gewurz, B. E. (2021) Epstein-barr virus induced cytidine metabolism roles in transformed B-cell growth and survival. *mBio* **12**, e0153021